Journal of the Mechanics and Physics of Solids 81 (2015) 22–40

Contents lists available at ScienceDirect

Journal of the Mechanics and Physics of Solids

journal homepage: www.elsevier.com/locate/jmps

Mechanics of wrinkle/ridge transitions in thin film/substrate systems

Lihua Jin [a,b], Atsushi Takei [c], John W. Hutchinson [a,*]

[a] School of Engineering and Applied Sciences, Harvard University, Cambridge, MA, USA
[b] Dept. of Civil and Environmental Engineering, Stanford University, Stanford, CA, USA
[c] Institute of Industrial Science, University of Tokyo, Tokyo, Japan

ARTICLE INFO

Article history:
Received 10 February 2015
Received in revised form
17 April 2015
Accepted 25 April 2015
Available online 7 May 2015

Keywords:
Wrinkling
Thin films
Elastic substrates
Ridge instabilities
Soft materials

ABSTRACT

The mechanics of the formation and propagation of ridges on compressed stiff film/compliant substrate systems is studied theoretically and experimentally. Ridges form on bilayer systems where the elastomeric substrate is subject to a significant pre-stretch prior to attachment of the film. When the bilayer is then subject to increasing overall compressive strain, sinusoidal wrinkles first form and subsequently become unstable giving way to localized ridges with relatively large amplitudes. Two-dimensional plane strain simulations for neo-Hookean film/substrate systems reveal the transition from wrinkles to ridges under increasing compression and the reverse transition from ridges to wrinkles when the overall compression is subsequently reduced. For a significant range of pre-stretch, the two transition strains differ, and a significant hysteresis response is observed in a complete cycle of loading and unloading. The Maxwell equal-energy condition has been identified associated with co-existence of wrinkles and ridges and with the three-dimensional steady-state propagation condition for the ridges. Experiments conducted with a specially designed film/substrate loading system have been performed that confirm the essential features of ridge formation and the hysteretic behavior in loading/unloading cycles that span the two transitions.

1. Introduction

When a stiff thin film supported by a compliant thick substrate is compressed to a critical strain, the flat surface loses stability and forms periodic wrinkles (Bowden et al., 1998; Nowinski, 1969). In recent years the notion that wrinkles are a failure mode which should be suppressed has been replaced by efforts to make creative use of wrinkles. Published efforts have included the fabrication of stretchable electronics (Khang et al., 2006), measurement of mechanical properties (Stafford et al., 2004), assembly of particles (Lu et al., 2007; Schweikart and Fery, 2009), changing optical properties (Kim et al., 2013; Lee et al., 2010), and tuning surface adhesion and wettability (Chan et al., 2008; Chung et al., 2007; Lin et al., 2008; Lin and Yang, 2009). The reversibility of the elastic deformation associated with wrinkling in these applications allows the systems to be repeatedly cycled between flat and wrinkle states. Various wrinkle morphologies have also been studied, such as sinusoidal, herringbone, checkerboard and hexagonal modes (Audoly and Boudaoud, 2008; Bowden et al., 1998; Cai et al., 2011), induced by varying the loading condition, such as from uniaxial to biaxial compression (Breid and Crosby, 2011), and

* Corresponding author.
E-mail address: jhutchin@fas.harvard.edu (J.W. Hutchinson).

http://dx.doi.org/10.1016/j.jmps.2015.04.016
0022-5096/

controlling the deterministic order of wrinkles (Lin and Yang, 2007; Yin et al., 2012).

After the formation of wrinkles, if the compressive strain is further increased, new advanced modes can appear such as wrinkles that double their periodicity and ultimately form localized folds (Brau et al., 2013, 2011; Holmes and Crosby, 2010; Kim et al., 2011; Pocivavsek et al., 2008; Sun et al., 2012). Only recently has it become apparent, that post-wrinkling bifurcations depend in a significant way on pre-stretch of the substrate (Auguste et al., 2014; Sun et al., 2012). If the substrate is subject to a tensile pre-stretch, wrinkles are stabilized and period-doubling does not usually occur until overall compressive strains of about 20% are imposed if the film/substrate modulus ratio is large (Auguste et al., 2014; Cao and Hutchinson, 2012; Chen and Crosby, 2014). The stabilized wrinkles grow to a relatively high aspect ratio (Chen and Crosby, 2014). If the substrate is subject to a mild pre-compression, wrinkles are destabilized and period-doubling occurs earlier at a lower overall compressive strain (Auguste et al., 2014). If the substrate is subject to a large pre-compression of around 0.3 strain, the wrinkle period appears to multiply chaotically (Auguste et al., 2014).

It has also been discovered that if the substrate is subject to a sufficiently large pre-tension prior to film attachment, a different mode of post-wrinkling can occur termed the localized ridge mode (Cao et al., 2014; Cao and Hutchinson, 2012; Takei et al., 2014; Wang and Zhao, 2013; Zang et al., 2012). In the two-dimensional context, one out of perhaps five or ten wrinkles grows to a large amplitude forming a ridge with the remaining wrinkles reduced to an almost flat state. Although folds and ridges are both localized, their morphologies are very different. A fold bends the film into a tight loop that pushes into the substrate, while a ridge is an open bend which grows outwards from the substrate pulling the substrate with it. These differing post-wrinkling behaviors can be explained qualitatively by the highly nonlinear elasticity of the elastomeric substrate. A significant pre-tension of the substrate makes it easier to pull material outward from the surface than to push material into the surface, while a pre-compression has the opposite effect (Cao and Hutchinson, 2012; Zang et al., 2012). The ridge instability mode was first noted in a numerical simulation (Cao and Hutchinson, 2012), and then shortly thereafter observed in experiments (Cao et al., 2014; Chen and Crosby, 2014; Takei et al., 2014; Wang and Zhao, 2013; Zang et al., 2012). The large aspect ratio of the ridge instability facilitates its applications in reversible wettability tuning and applications involving cell alignment (Cao et al., 2014).

It has been shown within a two-dimensional context that the wrinkle to ridge transition is unstable – that wrinkles will snap dynamically to ridges (Takei et al., 2014). However, the detailed mechanics of the formation and propagation of ridges has not been studied. In particular, the implications of the distinct wrinkle-to-ridge and ridge-to-wrinkle transitions and the associated hysteretic behavior under cycles of compression remain unclear. In this paper, we use the finite element method to study the formation, propagation, hysteresis and geometry of ridges. A detailed exploration of the two-dimensional behavior of ridges is given using plane strain simulations as depicted in Fig. 1a. These provide conditions for the transitions from wrinkles to ridges and vice versa, together with hysteric effects associated with cycles of compression which span the transitions. Based on arguments associated with the Maxwell condition for co-existing phases, these same two-dimensional simulations can be used to derive conditions governing the co-existence of wrinkles and ridges and for the three-dimensional steady-state propagation of the ridges, as depicted in Fig. 1b. The present study is purely mechanical and conducted within the framework of nonlinear continuum elasticity. The wrinkles and ridges can be interpreted as distinct phases and, as such, the system represents a mechanical realization of phase transitions within the larger setting of material phase transitions (Porter and Easterling, 1981; Balluffi et al., 2005). Parallels exist between the present system and martensitic phase transitions studied extensively in the materials and mechanics literature (e.g., Zhang et al., 2009). To simulate the wrinkle to ridge transition and its reverse, we have exploited two numerical techniques which will be described in the body of the paper: the static force–displacement method and pseudo-dynamic loading–unloading method.

Full details of the simulations for one particular case are presented in Section 2 introducing the definitions of the two transformation strains, the Maxwell strain and the hysteresis behavior under cyclic overall compression. The sensitivity of the computational model to some of the modeling assumptions is presented in Section 3 along with simulations which reveal the role of substrate pre-stretch and the redistribution of the energy in the wrinkle to ridge transition. Experimental results demonstrating ridge formation and cyclic loading hysteresis for a specific stiff film/substrate bilayer are obtained using a specially designed pre-stretching/compression system. These are presented in Section 4. Concluding remarks are given in Section 5.

2. Analysis of ridge formation, propagation and critical transitions

The formation and propagation of ridges in a film/substrate bilayer with both materials modeled as neo-Hookean is investigated in this section. As noted in the Introduction, a substantial pre-stretch of the substrate is required for ridges to form. In the simulations in this paper, both the pre-stretch and the subsequent overall compression of the bilayer are taken to be plane strain deformations. Two-dimensional wrinkle and ridge patterns with no out-of-plane variation are analyzed in detail using plane strain simulations, as described in the following subsections. These same simulations can be used to derive conditions for the three-dimensional co-existence of wrinkles and ridges and the steady-state propagation of ridges. In particular, the plane strain simulations enable the determination of the Maxwell condition governing the steady-state propagation of a ridge front at a critical overall compressive strain, cf., Fig. 1b. Thus, this paper will simultaneously address wrinkling/ridge transitions in the context of plane strain and three-dimensional ridge propagation and wrinkle/ridge co-existence.

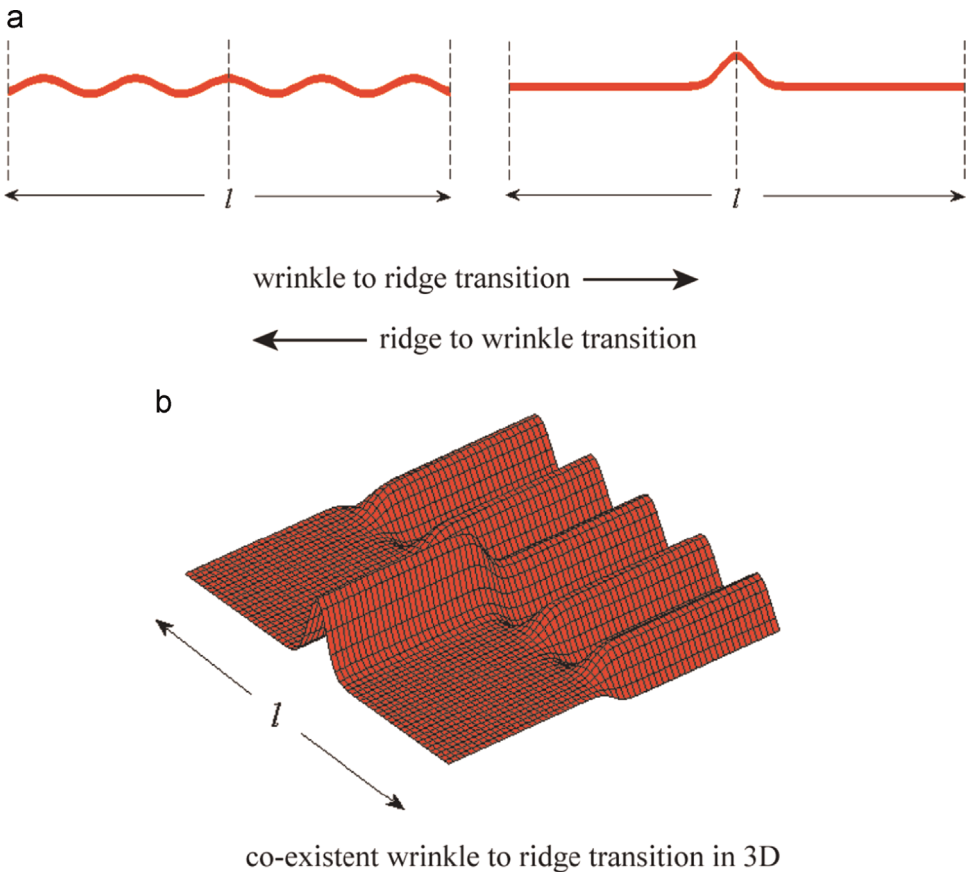

Fig. 1. (a) The computations in this paper analyze wrinkles and ridges in a bilayer consisting of a thin stiff film on a compliant deep substrate in two-dimensional plane strain. (b) A schematic of co-existent wrinkles and a ridge at the Maxwell strain. Quasi-static steady-state propagation of the ridge at its front is also possible at the Maxwell strain.

In the undeformed state, the substrate has a length L_0, and the film has a length L (Fig. 2a). The substrate is pre-stretched to length L, with pre-stretch $\lambda_0 = L/L_0$, and then bonded to the stress-free film (Fig. 2b). In the bonded state, the thicknesses of the film and substrate are h_f and h_s respectively. Then the bilayer is compressed together to the current length l, with the overall compressive strain defined as $\varepsilon = (L - l)/L$ (Fig. 2c). Both the film and substrate are considered to be incompressible neo-Hookean materials, with ground state moduli μ_f and μ_s respectively (Fig. 2a).

Under plane strain conditions, when the compressive strain ε is small, the surface is flat and the film and substrate are each subject to a homogeneous deformation. When ε reaches a critical value ε_w (which is a function of pre-stretch λ_0 and other parameters), the onset of wrinkling occurs (Fig. 2d). If λ_0 is sufficiently large, with the further monotonic increase of ε, the wrinkles transition to ridges at a critical compressive strain $\varepsilon_{w\to r}$ (Fig. 2e). It will be shown that the wrinkle to ridge transition is an unstable transition, with wrinkles snapping into ridges. Special numerical techniques are usually needed to simulate such transitions, and here two methods are employed for this purpose, introduced in turn in the next two sections. A specific thin film/deep substrate system with $\mu_f/\mu_s = 1000$ and pre-stretch $\lambda_o = 2$ is thoroughly analyzed to define and provide the critical strains associated with the system behavior.

2.1. The static force–displacement method

The finite element software ABAQUS is used to simulate the formation and growth of a ridge under plane strain conditions. A linear perturbation analysis is first conducted to identify the critical strain for wrinkle initiation ε_w and the associated critical wavelength l_w for a finite film/substrate model described in detail below which is wide and deep compared to l_w. To simulate a static process of compression and to break the translational symmetry beyond the onset of wrinkling an initial geometric imperfection is introduced. It has the form of an initial stress-free surface undulation in the shape of the critical wrinkle mode with a very small amplitude equal to 0.01 times the film thickness. A more detailed description of the prescribed imperfection is given later in Section 3.1. As the overall compressive strain increases above ε_w, the amplitude of each wrinkle peak becomes larger, but the number of wrinkles does not change nor does the uniformity of the wrinkle pattern. To search for ridge solutions, the "static force method" imposes an additional vertical displacement to

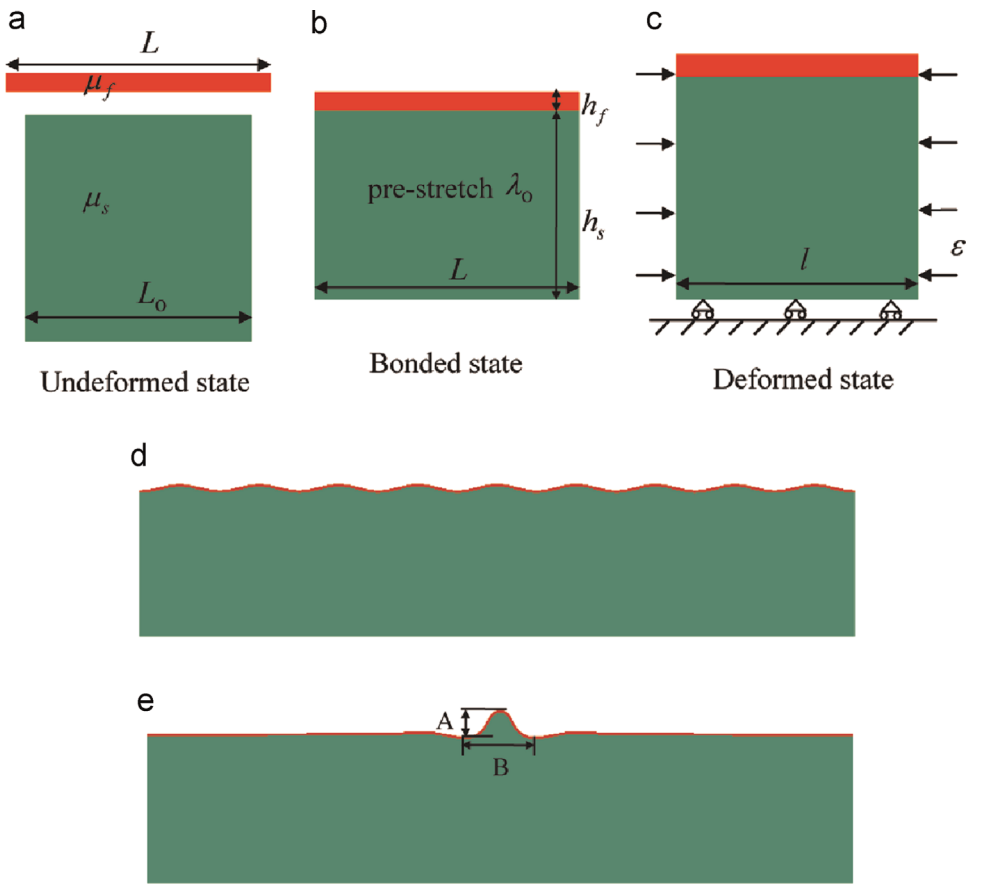

Fig. 2. A neo-Hookean film/substrate bilayer in different states. (a) In the undeformed state, the film has a length L and ground state modulus μ_f, while the substrate has a length L_0 and ground state modulus μ_s. (b) In the bonded state, the substrate is pre-stretched to length L, with pre-stretch $\lambda_0 = L/L_0$, and bonded with the stress-free film. (c) In the deformed state, both the film and substrate are compressed together by an overall compressive strain $\varepsilon = (L - l)/L$. (d) A simulation result of wrinkles at a strain just below the ridge to wrinkle transition strain $\varepsilon_{r\to w}$. (e) A simulation result of a localized ridge at a strain just above the wrinkle to ridge transition strain $\varepsilon_{w\to r}$. Only the upper quarter of the substrate is shown in (d) and (e).

the peak of one of the wrinkles to push the system towards an equilibrium ridge solution. Specifically, as illustrated by the example in Fig. 3a, at a sequence of fixed values of the strain $\varepsilon > \varepsilon_w$, an additional vertical displacement Δ is imposed on the peak of the central wrinkle. The associated reaction force per unit out-of-plane depth F together with the total elastic energy of model per unit out-of-plane depth U are computed as a function of Δ.

Before going into the details of the static force method, we describe the finite element model used to generate the results in Fig. 3. The computational boundary conditions are chosen to model periodic deformation modes with period L parallel to the interface in the undeformed state. Further, symmetry of the deformation mode with respect to $x = 0$ is assumed for the half-model analyzed with a finite element mesh in Fig. 3a. The simulations have been carried out with $L = 9l_w$, such that the width of the finite element model is $L/2$. The depth is set by $(h_f + h_s)/h_f = 200$. The depth of the substrate is more than enough compared to the wrinkle wavelength and the ridge width, B, to insure the surface wrinkles and ridges do not interact with the bottom of the substrate. The model depicted in Fig. 3a assumes zero horizontal displacement and zero shear traction on the left vertical edge. On the right vertical edge the shear tractions are zero and a prescribed uniform horizontal displacement is imposed to create the overall compression ε. The bottom of the substrate has zero vertical displacement and no shear traction. The top surface is traction-free apart from the probing displacement, Δ, which is imposed on the wrinkle peak at the left edge of the computational model. The pre-stretch of the substrate is implemented in a user-defined material subroutine UMAT. For the example in Fig. 3, the ratio of the ground state shear moduli of the neo-Hookean film and substrate is $\mu_f/\mu_s = 1000$. The critical strain for wrinkle initiation for this case is $\varepsilon_w = 0.0093$. By virtue of the boundary conditions of the model, any solution can be regarded having a periodicity of L and, in particular, when a ridge is found at the center of the finite element model the solution represents a periodic array of ridges with spacing L. The effect of the choice of period L is investigated in Section 3.

Return now to the details for the static force method for the case in Fig. 3 in which the substrate pre-stretch is $\lambda_0 = 2$. For different values of *fixed* overall compressive strains satisfying, $\varepsilon > \varepsilon_w$, the reaction force/depth F normalized by $\mu_s L$ is plotted as a function of the additional normalized imposed vertical displacement Δ/h_f (Fig. 3b). For the smaller values of ε, the $F - \Delta$

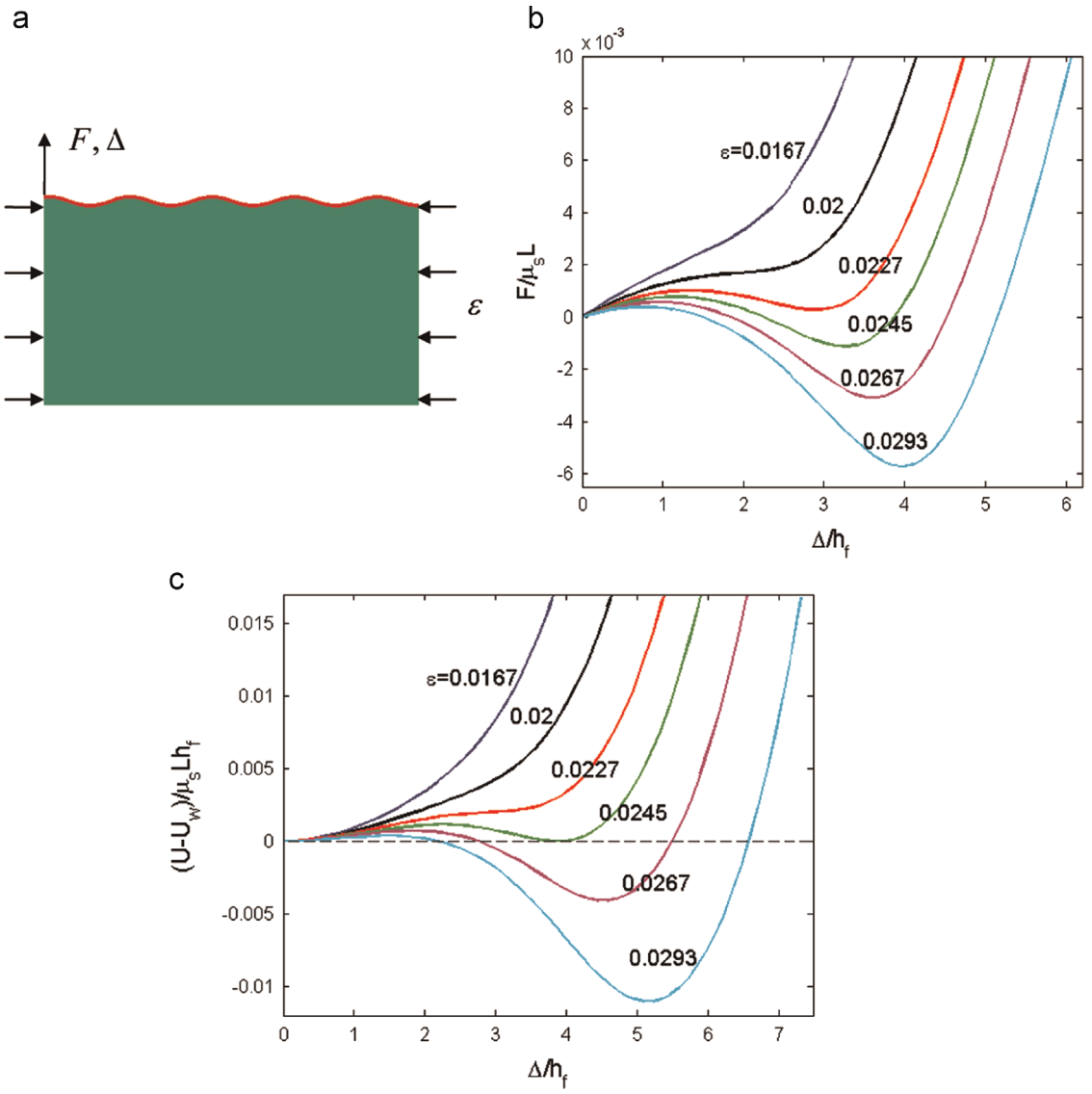

Fig. 3. The computation results from the static force–displacement method. (a) A schematic of the method showing the right half of the deformation period used in the finite element model. A film/substrate bilayer is subject to a strain $\varepsilon > \varepsilon_w$, and wrinkles form. Under the fixed strain ε, an additional vertical displacement Δ is prescribed at the peak of a wrinkle, and the reaction force F and the total elastic energy of the sample U are computed. (b) The reaction force F as a function of the vertical displacement Δ with pre-stretch $\lambda_0 = 2$ under various fixed compressive strains ε. (c) The elastic energy minus the elastic energy of the wrinkled state $U - U_w$ as a function of the vertical displacement Δ with the same pre-stretch and overall compressive strains as (b). The simulation results are for modulus ratio $\mu_f/\mu_s = 1000$, thickness ratio $(h_f + h_s)/h_f = 200$ and period $L = 9l_w$.

curve is monotonic, and F only vanishes at $\Delta = 0$. However, for somewhat larger ε, the $F - \Delta$ curve becomes non-monotonic, and for a range of ε, $\varepsilon_{r\to w} < \varepsilon < \varepsilon_{w\to r}$, the curves have two points with $F = 0$ at non-zero values of Δ. (For $\varepsilon > \varepsilon_{w\to r}$ there is only one non-zero value of Δ with $F = 0$, which is not shown in Fig. 3.) If a solution with zero F is found when Δ is non-zero, then that solution corresponds to an equilibrium state at the particular overall compression ε. The solution may be stable or unstable. In the sequel it will be shown that when $\varepsilon_{r\to w} < \varepsilon < \varepsilon_{w\to r}$, the first intersection of the $F - \Delta$ curve with $F = 0$ and $\Delta > 0$ corresponds to an unstable solution and the second such intersection is a stable ridge solution. The instability of the former can immediately be anticipated from the fact that probe extracts energy from the bilayer for small deviations from this state.

In summary, for $\varepsilon_{r\to w} < \varepsilon < \varepsilon_{w\to r}$, there are three points on the $F - \Delta$ curve with $F = 0$: (1) the point with $\Delta = 0$ is the wrinkle solution, (2) the intermediate point corresponds to a ridge-like solution that is unstable, and (3) the rightmost point corresponds to a stable ridge solution. As seen in Fig. 3b and as will be discussed later in more detail, the ridge amplitude is much larger than wrinkle amplitude at the same ε. Further, the ridge is a localization in the sense that the undulations on either side of the ridge have much smaller amplitudes than the wrinkles which preceded them.

Fig. 3c plots the dependence of the elastic energy/depth of the system U minus the elastic energy/depth of the wrinkle

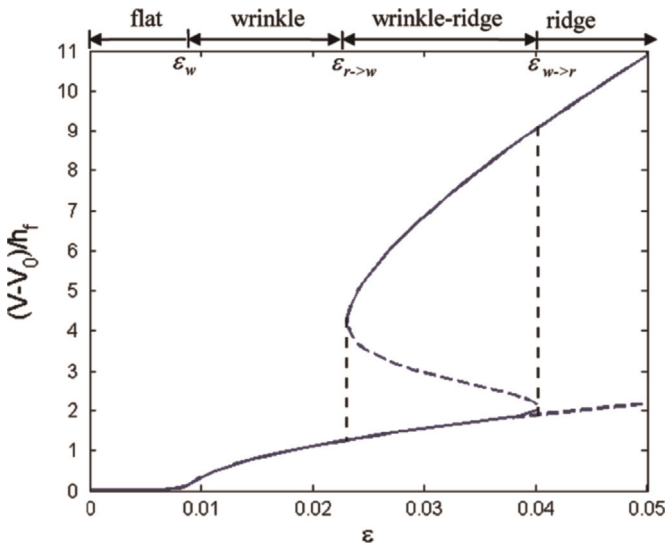

Fig. 4. Vertical displacement V of the ridge peak, minus the vertical displacement of the homogeneous deformation V_0, for all the equilibrium states as a function of ε. The dashed curve segments are states that are unstable to arbitrarily small disturbances or perturbations. The simulation results are for pre-stretch $\lambda_0 = 2$, modulus ratio $\mu_f/\mu_s = 1000$, thickness ratio $(h_f + h_s)/h_f = 200$ and period $L = 9l_w$.

state U_w, normalized by $\mu_s L h_f$, as a function of the vertical displacement Δ normalized by h_f for the same pre-stretch and compressive strains as Fig. 3b. When ε is small, the $F - \Delta$ curve is monotonic in Fig. 3b, and the wrinkle state with zero Δ is the only energy minimum in Fig. 3c. With an increase of ε, another (local) energy minimum at a non-zero Δ appears. The three intersections of the $F - \Delta$ curve with the Δ-axis in Fig. 3b correspond to the two energy minima (possibly local) and one energy maximum in Fig. 3c. The second energy minimum is associated with the ridge solution. A special situation occurs, which will be discussed later in some detail, when the two energy minima have the same value at an overall compression $\varepsilon_{Max} = 0.0245$, defined as the Maxwell strain. When $\varepsilon > \varepsilon_{Max}$, the energy of the ridge state is smaller than that of the wrinkle state, and vice versa.

In Fig. 4, the vertical displacement V of the ridge peak (top left corner of the computational model), minus the vertical displacement V_0 of the same system in the homogeneous deformation state, is plotted for all the equilibrium states as a function of ε for the same system described in Fig. 3. Fig. 4 is especially useful for introducing the wrinkle and ridge "phases" and the transitions between them. When $\varepsilon < \varepsilon_w$, $V - V_0 = 0$ and the surface is strictly flat, assuming no initial imperfection. When $\varepsilon_w < \varepsilon < \varepsilon_{r\to w}$, with $\varepsilon_{r\to w}$ as the plane strain ridge to wrinkle transition strain, wrinkles form and are the only equilibrium state. When $\varepsilon_{r\to w} < \varepsilon < \varepsilon_{w\to r}$, with $\varepsilon_{w\to r}$ as the plane strain wrinkle to ridge transition strain, there are three equilibrium states: the wrinkle state, the stable ridge state with the large amplitude (the upper solid curve), and the unstable ridge state with an intermediate amplitude (the dashed line). In plane strain, in the range $\varepsilon_{r\to w} < \varepsilon < \varepsilon_{w\to r}$, either the wrinkle state or the large amplitude ridge state can exist depending on the prior compression history, as discussed later. When $\varepsilon > \varepsilon_{w\to r}$, both the wrinkle state and the large amplitude ridge state are equilibrium states but the wrinkle state is unstable to arbitrarily small disturbances. The wrinkle bifurcation strain and two plane strain transition strains obtained for the set of conditions in Figs. 3 and 4 are $\varepsilon_w = 0.0093$, $\varepsilon_{r\to w} = 0.023$ and $\varepsilon_{w\to r} = 0.040$.

In Fig. 5a, the elastic energy U of the stable equilibrium states minus the elastic energy of the flat state U_0 is plotted as a function of ε for the same system discussed above. When $\varepsilon < \varepsilon_w$, $U = U_0$. When $\varepsilon > \varepsilon_w$, the wrinkle state has an elastic energy lower than the flat state. When $\varepsilon > \varepsilon_{r\to w}$, the large amplitude ridge state exists with energy that is also lower than the flat state. However, it is evident from Fig. 5a that the energy difference between the wrinkle and ridge states is small compared to their differences from the flat state. To better distinguish the energy difference between the wrinkle state and the ridge state, the energy difference of the ridge and wrinkle states, $U_r - U_w$, is plotted as a function of ε in Fig. 5b. The ridge state has a higher energy than the wrinkle state, i.e., $U_r - U_w > 0$, when the overall strain is lower than the Maxwell strain, $\varepsilon < \varepsilon_{Max}$, while the ridge state has a lower energy, i.e., $U_r - U_w < 0$, when $\varepsilon > \varepsilon_{Max}$. For this example, the Maxwell strain, $\varepsilon_{Max} = 0.0245$, is much closer to the ridge to wrinkle transition, $\varepsilon_{r\to w} = 0.023$, than to the wrinkle to ridge transition, $\varepsilon_{w\to r} = 0.040$.

With the insights from Figs. 3 to 5, we are now in a position to discuss the transitions in relation to imposed histories of overall compression ε and the expected hysteresis under cyclic histories. Consider first deformations constrained to be plane strain and a history in which ε increases monotonically from zero. The flat state gives way to the onset of wrinkles at $\varepsilon = \varepsilon_w$. The wrinkles are stable and grow in amplitude until $\varepsilon = \varepsilon_{w\to r}$ at which point the wrinkles become unstable and snap (dynamically) to the large amplitude ridge. The slight increase in the growth rate of the wrinkle amplitude seen in Fig. 4 just before $\varepsilon_{w\to r}$ is reached is believed to be associated with small numerical imperfections assumed in the analysis. For $\varepsilon > \varepsilon_{w\to r}$ only the ridge is stable, at least in the 2D context. Behavior of the ridge for strains significantly larger than $\varepsilon_{w\to r}$ has not been explored. The emphasis here has been primarily on the transitions. "Dynamic" simulations in the next section will reinforce

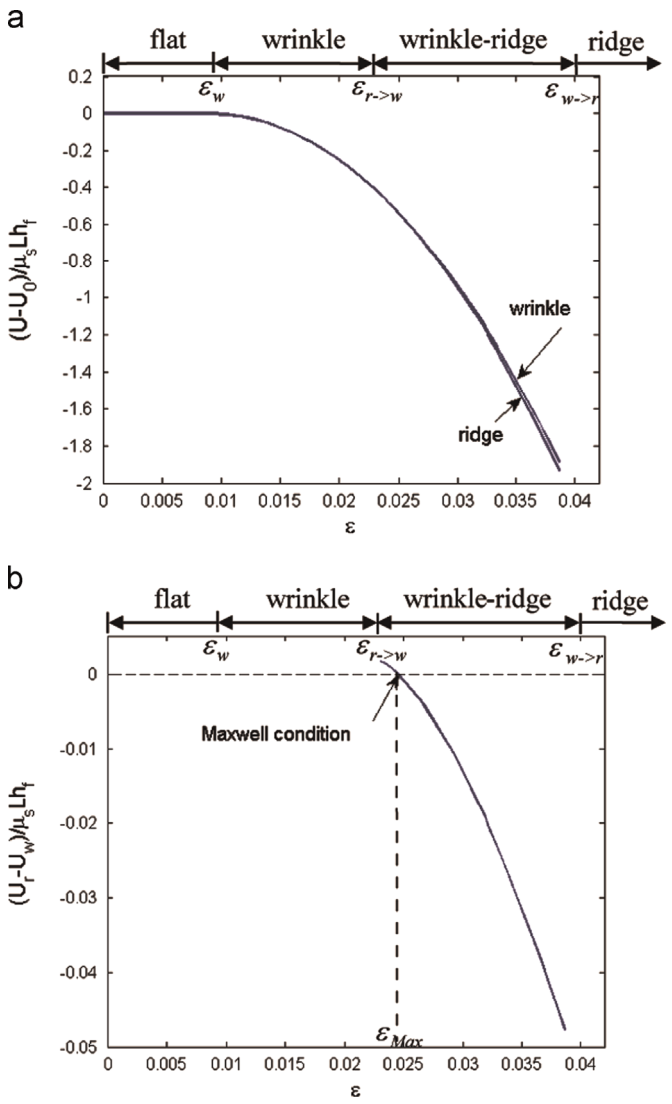

Fig. 5. (a) Elastic energy U of the stable equilibrium states minus the elastic energy of the flat state U_0 as a function of ε. Presented in this manner, the difference between the wrinkle and ridge states is not emphasized. Therefore, in (b) the energy difference between the ridge state and the wrinkle state $U_r - U_w$ is presented. At the Maxwell strain ε_{Max}, the ridge state and the wrinkle state have the same energy.

these assertions. Now, starting with $\varepsilon > \varepsilon_{w\to r}$, reduce the overall compression ε monotonically to zero. The ridge remains stable until $\varepsilon = \varepsilon_{r\to w}$ when the ridge becomes unstable and snaps (dynamically) to wrinkles. In Fig. 4 it can be seen that the ridge solution at $\varepsilon = \varepsilon_{r\to w}$ is a limit point with no ridge solutions existing for $\varepsilon < \varepsilon_{r\to w}$. As ε is further reduced to zero, the wrinkles reduce in amplitude until they vanish in the range $\varepsilon < \varepsilon_w$.

As long as three dimensional imperfections or disturbances do not disrupt the plane strain deformations, cycles of ε starting below $\varepsilon_{r\to w}$ and ending above $\varepsilon < \varepsilon_{w\to r}$ will follow the loop (cf., Fig. 4) defined by wrinkles transitioning to ridges with increasing ε at $\varepsilon_{w\to r}$ and, subsequently, ridges transitioning back to wrinkles with decreasing ε at $\varepsilon_{r\to w}$. Hysteresis is associated with the difference between $\varepsilon_{w\to r}$ and $\varepsilon_{r\to w}$, and the fact that one transition occurs under increasing ε and the other occurs under decreasing ε.

It is important to be cognizant of the fact that the transitions and hysteresis behavior discussed in connection with Fig. 4 are limited to plane strain deformations. Within the context of three dimensions an imperfection or disturbance can disrupt plane strain behavior. If $\varepsilon > \varepsilon_{Max}$ and if a significant local disturbance nucleates a ridge, then the possibility exists that incipient ridge may propagate replacing wrinkles over a large area. At the Maxwell condition, with $\varepsilon = \varepsilon_{Max}$, the wrinkle state and the ridge state have the same energy and, in principle, can coexist as illustrated schematically in Fig. 1b. Under such conditions, if ε is then increased above ε_{Max}, the ridge advances engulfing wrinkles, while if ε reduced below ε_{Max} the wrinkles advance replacing the ridge.

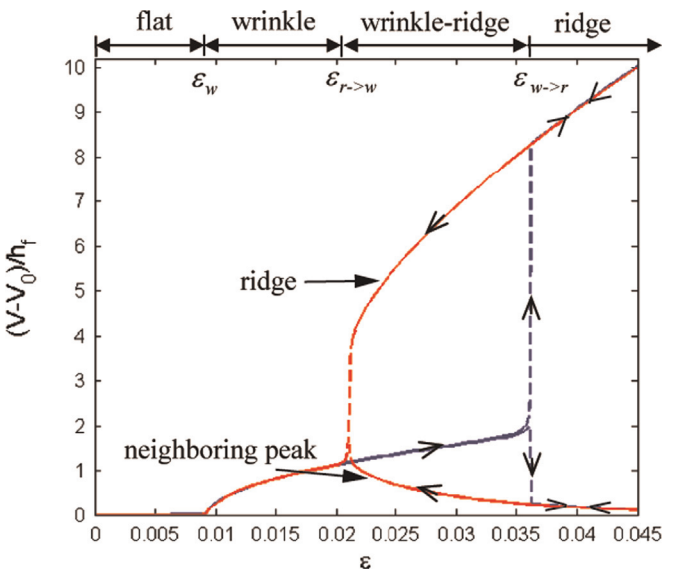

Fig. 6. The vertical displacements V of the ridge peak and its neighboring wrinkle peak as a function of strain ε as computed by the pseudo-dynamic method. Arrows directed to the right represent loading (ε increasing) while those directed to the left represent unloading (ε decreasing). During loading, one wrinkle snaps to a ridge with large amplitude at $\varepsilon_{w\to r}$, while the vertical displacement of the neighboring wrinkle peak diminishes significantly. During unloading, the ridge snaps back to the wrinkle state at $\varepsilon_{r\to w}$ and the vertical displacements of the neighboring wrinkles converge to the same value.

2.2. Pseudo-dynamic loading–unloading method

In this section the second method, pseudo-dynamic loading–unloading, is used to study the transitions within the plane strain context. The example analyzed is the same as in the previous section on the static force–displacement method with the same finite element mesh. As in the case of the static method, a linear perturbation analysis is first carried out to identify the critical wrinkle mode. A very small imperfection is again introduced to promote both wrinkles and ridges, as described later. In the pseudo-dynamic method, inertial effects are neglected and each incremental step is static. However, velocity-dependent damping is introduced such that when loss of stability occurs, which would normally be accompanied by dynamic snapping, the damping provides numerical stabilization and allows the snap-through process to take place transitioning to another stable equilibrium state. Artificial damping is a computational ploy that allows the computation to pass through the unstable transition from wrinkles to ridges. The viscous force in the equilibrium equations associated with the damping is defined as a damping factor times the nodal velocity times an artificial mass matrix with unit density; the damping factor in the calculations was set as 0.0002.

The system with substrate pre-stretch $\lambda_0 = 2$ is first compressed monotonically from $\varepsilon = 0$ to an overall strain $\varepsilon = 0.045$ that is larger than the wrinkle to ridge transformation strain, $\varepsilon_{w\to r}$, and then unloaded monotonically back to $\varepsilon = 0$. The vertical displacements V of the ridge peak and its neighboring wrinkle peak are recorded in Fig. 6. The progression along the curves in the loading and unloading segments of the history is indicated by the direction of the arrows. During loading, the surface remains flat in the range, $0 < \varepsilon < \varepsilon_w$, wrinkles in the range $\varepsilon_w < \varepsilon < \varepsilon_{w\to r}$, and transitions to a ridge at $\varepsilon = \varepsilon_{w\to r}$. The vertical displacements of the ridge peak and its neighboring wrinkle peak coincide when $\varepsilon < \varepsilon_{w\to r}$. At the wrinkle to ridge transition strain, $\varepsilon_{w\to r}$, the wrinkles become unstable, and "snap" to form a localized ridge. Simultaneously, as part of the process, the peak of the neighboring wrinkle diminishes abruptly. In the localization process, the additional length of the film required to form the ridge is scavenged from the neighboring wrinkles, thereby reducing their amplitudes. The snapping process is represented by vertical dashed lines. In this example, the amplitude of the ridge peak right after the transition is more than four times the preceding wrinkle amplitude and the neighboring wrinkle amplitude is reduced by more than a factor of four. With the further increase of ε, the amplitude of the ridge peak continues to increase, while that of the neighboring wrinkle decreases.

The sequence of behaviors under monotonic unloading from $\varepsilon = 0.045$ to $\varepsilon = 0$ is also evident in Fig. 6. In the range, $\varepsilon > \varepsilon_{w\to r}$, the solution is reversible and identical to that during loading. In the range, $\varepsilon_{r\to w} < \varepsilon < \varepsilon_{w\to r}$, the ridge solution prevails. Thus, as noted in connection with the first solution method, there is significant hysteresis in the range, $\varepsilon_{r\to w} < \varepsilon < \varepsilon_{w\to r}$, with wrinkles prevailing during loading and ridges occurring during unloading. At $\varepsilon_{r\to w}$, the ridge state snaps back to the wrinkle state, and in the range, $\varepsilon < \varepsilon_{r\to w}$, the wrinkle solution is again reversible, coinciding with the loading solution.

The solution obtained by the pseudo-dynamic method show good agreement with the static method. The transition strains obtained by the pseudo-dynamic method are $\varepsilon_{r\to w} = 0.0212$ and $\varepsilon_{w\to r} = 0.0361$. Fig. 2d shows the simulation result of the wrinkle state just below $\varepsilon_{r\to w} = 0.0212$, and Fig. 2e shows the ridge state just above $\varepsilon_{w\to r} = 0.0361$. The transition strains

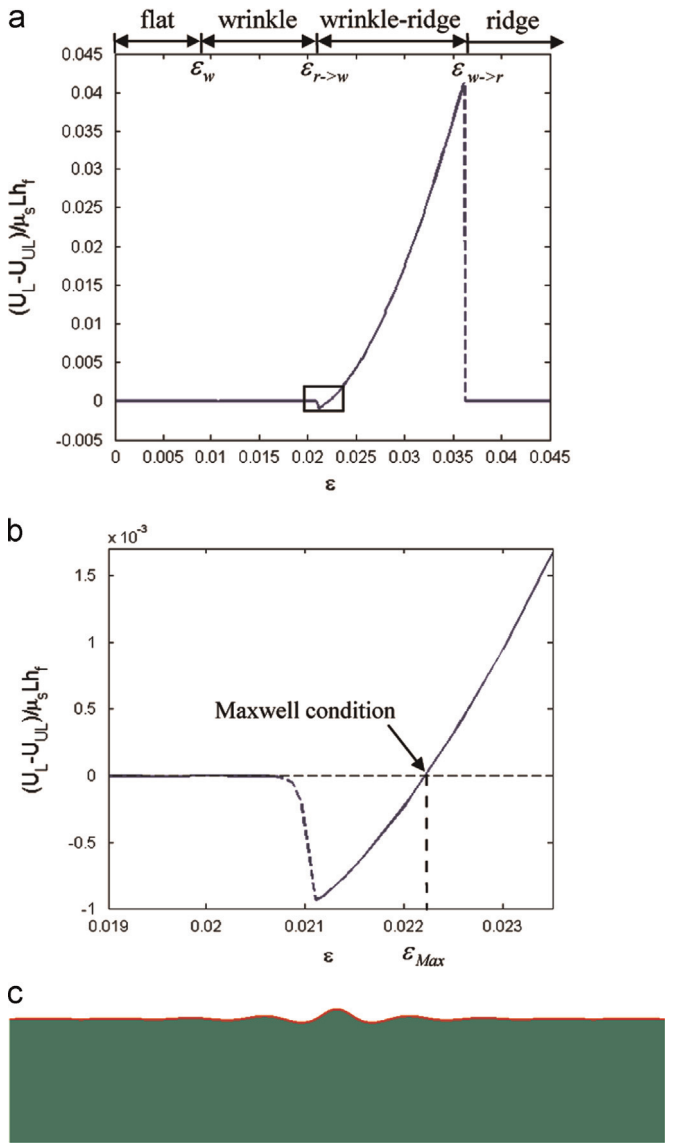

Fig. 7. (a) The elastic energy difference between the loading and unloading states $U_L - U_{UL}$ in Fig. 6 as a function of strain ε as computed by the pseudo-dynamic method. In the range $\varepsilon_{r\to w} < \varepsilon < \varepsilon_{w\to r}$, this is also the difference between the energy in the wrinkle state and the ridge state, $U_w - U_r$. The Maxwell condition is defined by the point when $U_L = U_{UL}$. (b) The amplification of the range of (a) containing the Maxwell strain. (c) The ridge state at the Maxwell strain ε_{Max} displayed for the full period. The results are for pre-stretch $\lambda_0 = 2$, modulus ratio $\mu_f/\mu_s = 1000$, thickness ratio $(h_f + h_s)/h_f = 200$ and period $L = 9l_w$.

from the pseudo-dynamic method are reasonably close to the values obtained by the static method ($\varepsilon_{r\to w} = 0.023$, $\varepsilon_{w\to r} = 0.040$). The reason for the small discrepancy between the two methods is most likely the artificial numerical damping introduced in the pseudo-dynamic method.

Further insights are obtained from examining the difference in the elastic energy in the system between the loading and unloading states, $U_L - U_{UL}$, associated with the hysteresis cycle. This difference is plotted as a function of overall compressive strain ε in Fig. 7a. When $\varepsilon < \varepsilon_{r\to w}$ or $\varepsilon > \varepsilon_{w\to r}$, the energies coincide $U_L - U_{UL} = 0$ because only one stable solution exists. However, when $\varepsilon_{r\to w} < \varepsilon < \varepsilon_{w\to r}$, a significant difference in energies exist reflecting the difference in energy between the wrinkle and ridge states in plane strain.

The computed differences obtained by this method are close to the ones obtained by the static method. The Maxwell condition is given by the point in the range $\varepsilon_{r\to w} < \varepsilon < \varepsilon_{w\to r}$ where $U_L = U_{UL}$, or, equivalently, $U_w = U_r$. Fig. 7b magnifies the region close to the Maxwell condition. The Maxwell strain obtained by the pseudo-dynamic method is $\varepsilon_{Max} = 0.0222$, which is close to the value obtained by the static method, $\varepsilon_{Max} = 0.0245$. When $\varepsilon < \varepsilon_{Max}$, the wrinkle state has the lower energy, while when $\varepsilon > \varepsilon_{Max}$, the ridge state's energy is lower. As noted earlier, the Maxwell strain is only slightly above the ridge to wrinkle transition strain and, as evident from Fig. 7a, the ridge state has substantially lower energy than the wrinkle state

over most of the range $\varepsilon_{Max} < \varepsilon < \varepsilon_{w\to r}$. Fig. 7c shows the simulation result of the ridge state at the Maxwell condition ε_{Max}.

The pseudo-dynamic loading–unloading method reproduces all the stable equilibrium solutions obtained by the static force–displacement method. Although the introduction of the numerical dissipation may slightly affect the solutions near the transition points, the pseudo-dynamic method is considerably more efficient than the static method. To obtain the critical transition strains, $\varepsilon_{r\to w}$ and $\varepsilon_{w\to r}$, and the Maxwell strain, ε_{Max}, only one loading/unloading simulation is required using the pseudo-dynamic method, while multiple simulations are needed if the static method is employed, with considerably more intervention on the part of the analyst. Therefore, most of the results presented in the remainder of this paper have been obtained using the pseudo-dynamic method.

3. The role of system parameters on transitions and Maxwell strain

In this section results will be presented to reveal how some of the system parameters, particularly the substrate pre-stretch λ_0, influence the critical transition strains and the Maxwell strain. In addition, further details of the ridges will be reported including the manner in which they redistribute the strain energy in the film layer and the substrate to lower the overall energy of the system. The first section reports an investigation into the sensitivity of the results to some of the modeling assumptions, including the assumed periodicity of the ridges and the slight initial imperfections.

3.1. Sensitivity to overall periodicity length and initial imperfections

In all the plane strain simulations reported above, periodic boundary conditions have been imposed on the computational model whose width is 9 times of the wavelength of the critical wrinkle mode, $L = 9l_w$. A very slight imperfection promotes the formation of a single ridge centered within this width. Thus, the ridge solutions discussed in the previous section correspond to a periodic ridge mode with period $L = 9l_w$. The effect of changing the overall period on the Maxwell strain is seen in Fig. 8a. The other system parameters and the initial imperfections have not been changed. The Maxwell strain ε_{Max} decreases with the increase of the ridge spacing for both the static and pseudo-dynamic methods with a discrepancy between the two predictions which is nearly constant. We expect ε_{Max} to approach a plateau when L/l_w becomes sufficiently large. However, the plateau associated with the smallest Maxwell strain at which a ridge can exist in a very large system has clearly not been reached in the range plotted in Fig. 8a, $6 \le L/l_w \le 18$. Thus, there is some sensitivity to the assumed width of the computational model. The remaining computations will be made with $L = 9l_w$, which represents a reasonable balance between computational efficiency and accuracy, but the sensitivity to overall periodicity must be borne in mind.

The effect of the size of initial imperfections on the critical transition strains and the Maxwell strain is illustrated in Fig. 8b, as obtained by the pseudo-dynamic method. In the simulations, the overall width of the model L is divided into half with a symmetry condition at the left end. The initial imperfection is a stress-free initial undulation of the system consisting of two components. The first component is in the shape of the first mode, the sinusoidal wrinkle, with amplitude δ, phased such that the initial displacement of the surface at the left end is δ. The second component is in the shape of the second mode with amplitude $\delta/2$, and it is phased such that its contribution to the initial surface displacement at the left end is $\delta/2$. The combined contributions have an initial surface displacement $3\delta/2$ at the left end of the model, i.e., at the center of the full period, and this is the point where the initial surface undulation is the largest. Thus, the two-component initial imperfection promotes both wrinkles and a ridge centered at the left end of the model.

Fig. 8b shows the dependence of the three strains, $\varepsilon_{r\to w}$, ε_{Max}, and $\varepsilon_{w\to r}$, on the normalized imperfection amplitude over the range of very small imperfections, $5\times10^{-4} \le \delta/h_f \le 5\times10^{-3}$. While $\varepsilon_{r\to w}$ and ε_{Max} display only modest sensitivity to the imperfection amplitude, the wrinkle to ridge transition strain, $\varepsilon_{w\to r}$, displays the fairly strong sensitivity to small imperfections expected for a system at an unstable bifurcation point (Budiansky, 1974; van der Heijden, 2009). The wrinkle to ridge bifurcation is asymmetric in the ridge amplitude and consequently the asymptotic relation between the transition and the imperfection is expected to have the form $\varepsilon_{w\to r} = \varepsilon^0_{w\to r} - c\ (\delta/h_f)^{1/2}$ where $\varepsilon^0_{w\to r}$ is the bifurcation strain of the perfect system. By fitting this relation to the numerical results for the two smallest imperfections, we obtained the asymptotic relation included in Fig. 8b with $c = 0.195$ and $\varepsilon^0_{w\to r} = 0.0404$. As is often the case, the range of validity of the asymptotic result is limited to quite small imperfections.

All the results obtained by the pseudo-dynamic method elsewhere in this paper have been based on the two-component imperfection with $\delta/h_f = 5\times10^{-4}$. The simulations carried out using the static method do not require the introduction of an imperfection component in the shape of the second mode because the imposition of the prescribed vertical displacement Δ at the left end of the model promotes the ridge at that location.

3.2. The influence of the substrate pre-stretch on the critical strains

Fig. 9a presents the effect of substrate pre-stretch λ_0 on the four critical strains, and Fig. 9b displays the width and height of ridges just before their transitions to wrinkles and right after their transitions from wrinkles, calculated using the pseudo-dynamic method. Only a limited range of pre-stretch has been explored and, in particular, no attempt has been made to determine lower limit of substrate pre-stretch at which ridges form, although earlier plane strain simulations place this

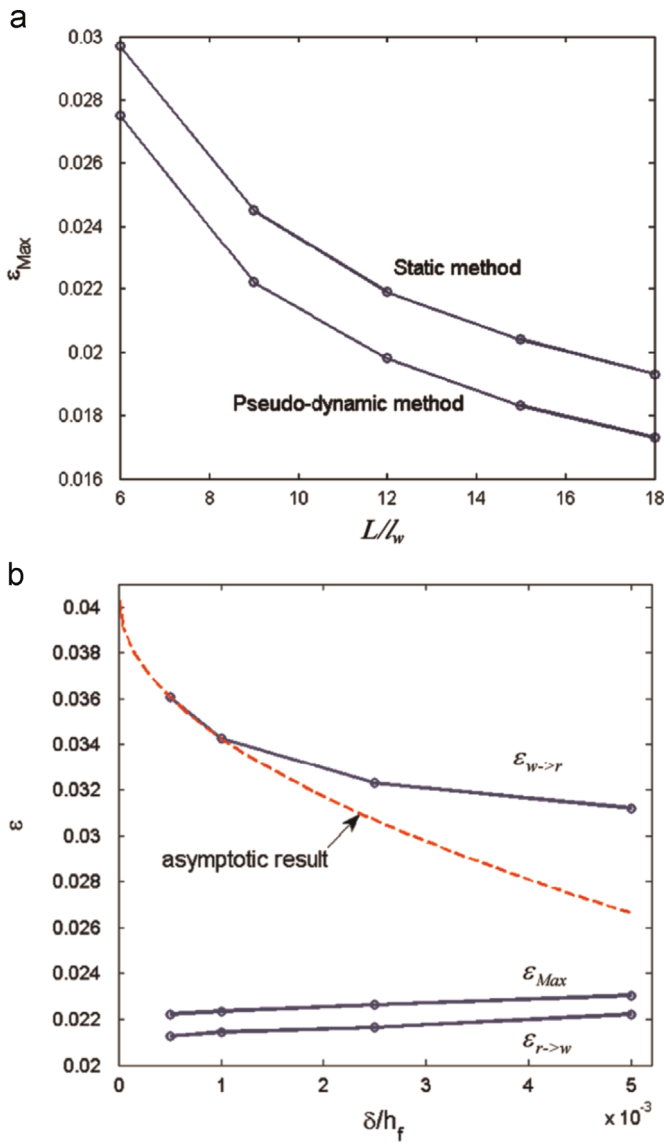

Fig. 8. (a) Effect of the solution periodicity L/l_w on the Maxwell strain ε_{Max} as predicted by the two methods. (b) Effect of the normalized imperfection size δ/h_f on the transition strains and the Maxwell strain as computed by the pseudo-dynamic method. The wrinkle to ridge transition is highly imperfection-sensitive because the perfect system has an asymmetric bifurcation. The asymptotic relation for sufficiently small imperfections is shown, determined as discussed in the text. The simulation results are for pre-stretch $\lambda_0 = 2$, modulus ratio $\mu_f/\mu_s = 1000$, thickness ratio $(h_f + h_s)/h_f = 200$ and period $L = 9l_w$.

lower limit at roughly $\lambda_0 \cong 1.4$ for neo-Hookean bilayers (Cao and Hutchinson, 2012). As shown in Fig. 9a, the critical strain for the initiation of wrinkles ε_w increases slightly with increasing λ_0, while the two transition strains and the Maxwell strain diminish and appear to converge to a common value at $\lambda_0 \cong 2.2$. However, simulations carried out with slightly larger pre-stretch, $\lambda_0 = 2.5$, reveal that there is still a small hysteresis range. We suspect that for pre-stretches above some value, ridges will form, but the hysteretic character of the transitions upon loading and unloading will be lost, however, our simulations have not fully established this conjecture. An example discussed in Section 3.4 for another constitutive model reveals that ridges can indeed form without hysteresis with a wrinkle to ridge transition that is stable. As shown in Fig. 9b, the width B and height A (cf. definitions in Fig. 2e) of the ridge just after the wrinkle to ridge transition decrease rather strongly with increasing λ_0, while these same quantities just before the ridge to wrinkle transition show less dependence on pre-stretch. In this example with $\mu_f/\mu_s = 1000$, the aspect ratio of the ridge falls roughly in the range $0.2 < A/B < 0.5$.

3.3. *The geometry and strain energy distributions in ridges and wrinkles*

In this section, selected results of the simulations are presented which provide further insight into the energetic driving force underlying transitions from wrinkle to ridge and the reverse transition.

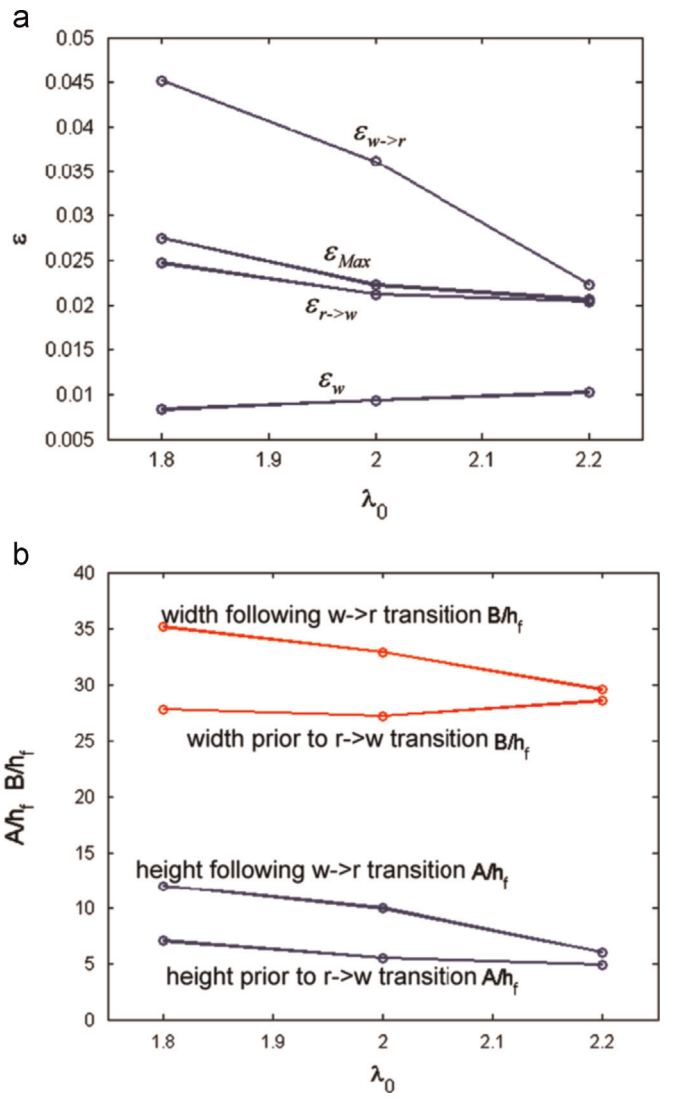

Fig. 9. (a) The dependence of the strain at the onset of wrinkling ε_w, the two transition strains and the Maxwell strain on substrate pre-stretch λ_0. (b) The dependence of the width and height of ridges (cf., Fig. 2e) on substrate pre-stretch λ_0 following and prior to the transition strains. The simulation results are for the modulus ratio $\mu_f/\mu_s = 1000$, the thickness ratio $(h_f + h_s)/h_f = 200$, and period $L = 9l_w$.

The variations of the ridge height A and width B as defined in Fig. 2e are shown in Fig. 10 over the range of ε from $\varepsilon_{r\to w}$ to well above $\varepsilon_{w\to r}$. The height increases with increasing ε while the width decreases. The aspect ratio of the ridge is approximately 1/2 at $\varepsilon = 0.045$, 1/3 at $\varepsilon_{w\to r} = 0.036$ and 1/5 at $\varepsilon_{r\to w} = 0.021$. Note that the height of the ridge is much larger than the wrinkle height at the corresponding overall compression, e.g., in this example the ridge height is roughly 4 times that of the wrinkle, as seen from Fig. 6.

In Fig. 11, the elastic energy differences between the wrinkle state and the ridge state, $U_w - U_r$, in the film and in the substrate, respectively, are plotted in the strain range $\varepsilon_{r\to w} < \varepsilon < \varepsilon_{w\to r}$, for the case with $\mu_f/\mu_s = 1000$, $(h_f + h_s)/h_f = 200$ and $\lambda_0 = 2$. This energy difference, $U_w - U_r$, can also be regarded as the energy difference in the film and substrate between the loading and unloading branches of the hysteresis loop discussed earlier. The sum of the contributions from the film and the substrate is the total energy difference between the wrinkle and ridge states of the entire system discussed earlier in Fig. 7. In the strain range, $\varepsilon_{r\to w} < \varepsilon < \varepsilon_{w\to r}$, when both wrinkles and ridges can exist, the elastic energy of the film is always higher in the wrinkle state than the ridge state, while the elastic energy of the substrate is only higher in the wrinkle state than in the ridge state when the overall compression strain is the upper portion of the range; it is lower in the wrinkle state in the lower portion of the range. As discussed earlier, below the Maxwell strain, $\varepsilon_{Max} \cong 0.0223$, the total energy is lower in the wrinkle state. Above the Maxwell strain, the total energy is lower in the ridge state, but there is a range ($\varepsilon_{Max} < \varepsilon < 0.0287$) in which energy in the substrate is still greater in the ridge state than in the wrinkle state. The existence of a ridge in this range relies on the tradeoff between the energy in the film and that in the substrate. At strains above $\varepsilon = 0.0287$, the energies of both the film and substrate are reduced in the ridge state relative to the wrinkle state. The fact that upon loading

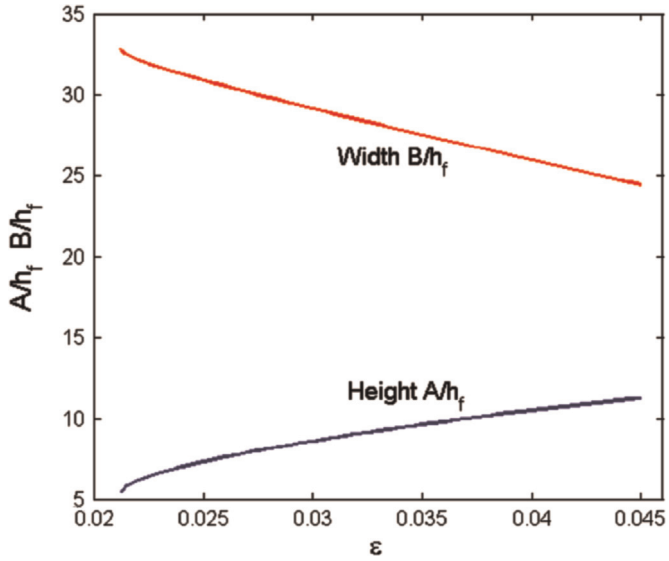

Fig. 10. The variation of the normalized width B and height A of the ridge (cf., Fig. 2e) as a function of strain ε for $\mu_f/\mu_s = 1000$, $(h_f + h_s)/h_f = 200$, $\lambda_o = 2$ and period $L = 9l_w$.

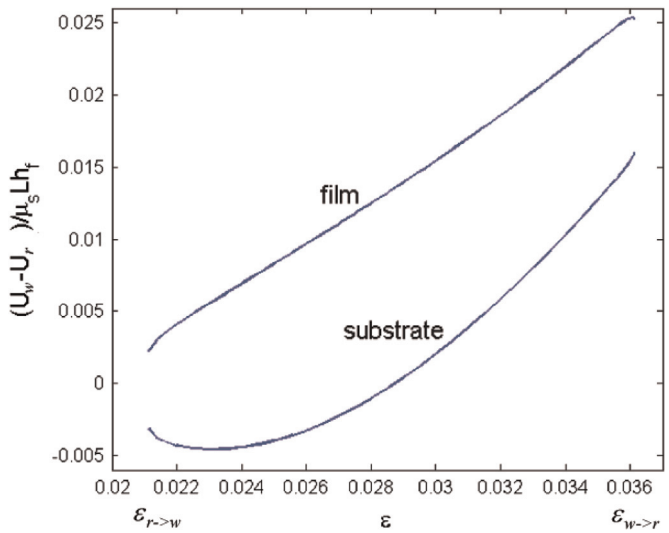

Fig. 11. The elastic energy differences between the wrinkle state and ridge state $U_w - U_r$ in the film (top curve) and substrate (bottom curve) in the strain range $\varepsilon_{r\to w} < \varepsilon < \varepsilon_{w\to r}$, with $\mu_f/\mu_s = 1000$, $(h_f + h_s)/h_f = 200$, $\lambda_0 = 2$ and period $L = 9l_w$.

wrinkles occur until ε attains $\varepsilon_{w\to r} = 0.036$, even though the ridge state has lower energy, is due the energy barrier between the two states which provides the stability of the wrinkle state well beyond the Maxwell strain.

Now we take a close look at the energy distributions in the substrate and film. We investigate the distribution of the elastic energy density ψ in the wrinkle and ridge states just above and just below the wrinkle to ridge transition, $\varepsilon_{w\to r} = 0.036$, with $\mu_f/\mu_s = 1000$, $(h_f + h_s)/h_f = 200$ and $\lambda_0 = 2$ (Fig. 12). When the system is in the ridge state (Fig. 12b), away from the ridge peak at distances somewhat greater than the peak width B, the system sustains a piecewise uniform deformation corresponding the uniform deformation of the film and that of the substrate under the pre-stretch and the external strain. Since the substrate is highly pre-stretched in the bonded state, its far field is subject to a large tensile strain. However, due to the formation of the ridge, the out-of-plane bulge superimposes compressive strain in the horizontal direction in the region below the peak of the ridge, which cancels much of the pre-tension in the substrate. Therefore, the elastic energy density in a dumbbell-shaped region below the peak of the ridge is much smaller than the value in the far field. Just below the film in the substrate on either side of the ridge is a region of intense shear with the highest energy density. The shear is created by the motion of the film on either side of the ridge feeding toward the ridge peak to provide the extra length of film required for ridge formation. All the elements of the mesh have rectangular shape in the state when the film is bonded. The intense shear in the substrate is evident from the shape of the elements that the top of the substrate

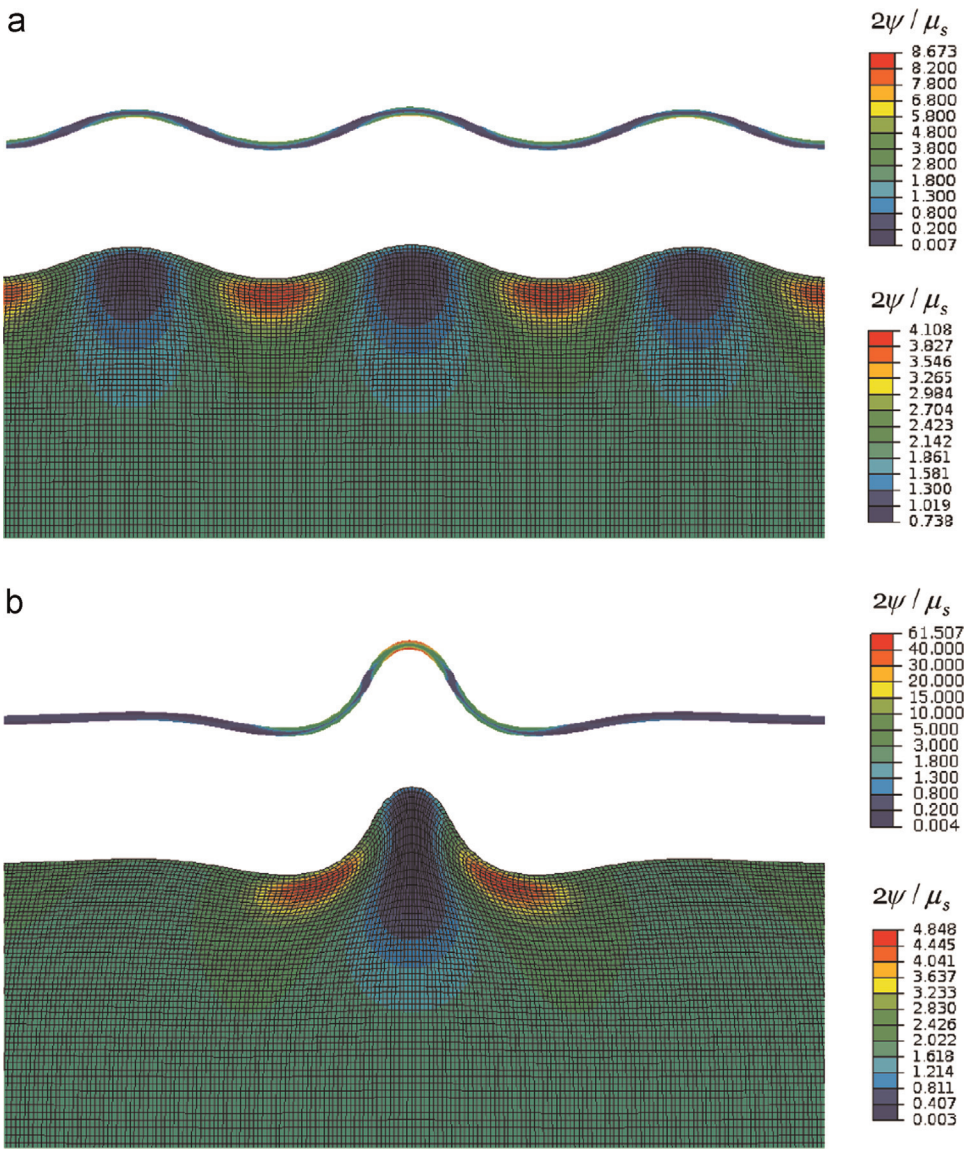

Fig. 12. Distribution of the elastic energy density in the film and the substrate at the wrinkle to ridge transition, $\varepsilon_{w\to r} = 0.036$, in the wrinkled (a) and in the ridge state (b). In this case, $\mu_f/\mu_s = 1000$, $(h_f + h_s)/h_f = 200$ and $\lambda_0 = 2$. Only the upper quarter of the substrate is shown.

in these regions. As a comparison, Fig. 12a shows the distribution of the elastic energy density ψ in the substrate for the wrinkle state under the same strain $\varepsilon_{w\to r} = 0.036$. The energy density is lower in the peaks of the wrinkles, while higher in the troughs of the wrinkles. The energy density maximum in the wrinkle state is lower than the ridge state, but the total energy minimum in the wrinkle state is much higher than that in the ridge state. Due to the high non-linearity of the neo-Hookean model under large pre-stretch, the localized ridge mode reduces the total energy from the wrinkle state.

Fig. 12 also shows the elastic energy distributions in the film for the ridge and wrinkle states respectively at the same strain $\varepsilon_{w\to r}$. Similar to the situation for the substrate, the maximal value of the energy density ψ in the ridge state is higher than the wrinkle state. By forming a localized ridge, although the peak of the ridge has a much higher ψ than the peak of the wrinkles, most of the film undergoes flattening in the ridge state and has lower ψ. The total elastic energy in the film is reduced when the ridge forms.

3.4. *The influence of strain-stiffening effect on the formation of ridges*

Polymers usually show a strain-stiffening effect when they are deformed close to their stretch limits. Since the neo-Hookean material model is based on the assumption that the end-to-end distance of the polymer chains satisfies a Gaussian distribution, it does not adequately represent the constitutive behavior of polymers under strains close to their stretch

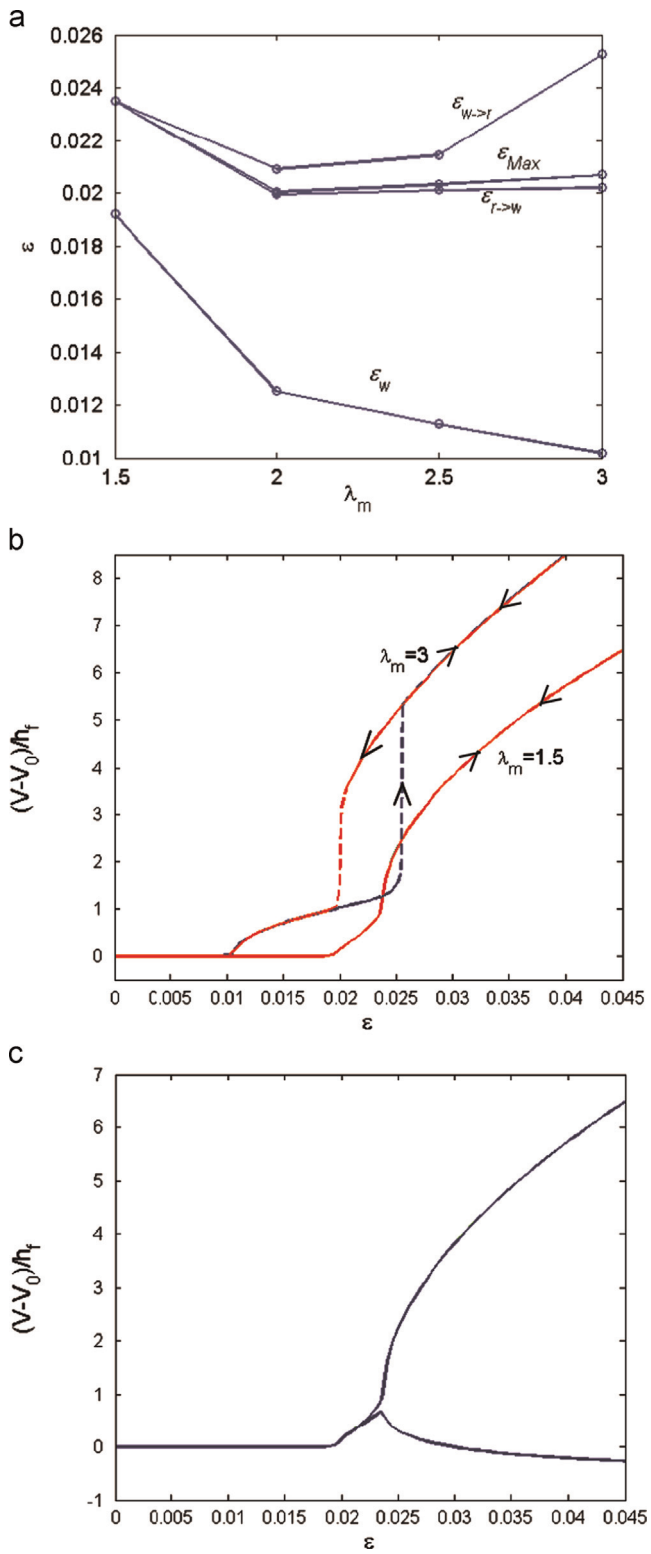

Fig. 13. The influence of the strain-stiffening effect on the formation or ridges. (a) The dependence of the strain at the onset of wrinkling ε_w, the two transition strains, and the Maxwell strain for ridges on the limit stretch of the substrate λ_m, with the substrate modeled as an Arruda–Boyce material. (b) The vertical displacement relative to the displacement under uniform deformation $V - V_0$ of the ridge peak as a function of strain ε during loading and unloading for $\lambda_m = 3$ and 1.5. The loading and unloading shows no hysteresis for $\lambda_m = 1.5$. (c) The relative vertical displacements $V - V_0$ of the ridge peak and its neighboring wrinkle peak as a function of strain ε for $\lambda_m = 1.5$, illustrating the onset of ridge localization and the absence of hysteresis. For all the simulations, the other parameters are set as $\mu_f/\mu_s = 1000$, $(h_f + h_s)/h_f = 200$, $\lambda_0 = 2$ and period $L = 9l_w$.

limits, and it does not accurately capture the strain-stiffening effect. For ridges to form, the substrate of the bilayer is under a relatively large pre-stretch and the formation of a ridge will further increase the strain in portions of the substrate. One can therefore expect the strain-stiffening to play a role in the formation of ridges if the pre-stretch of the substrate is close to the stretch limit of the polymer. In this section, we study the influence of the strain-stiffening effect on the formation of ridges.

In order to capture the strain-stiffening effect, we use the Arruda–Boyce material to model the substrate (Arruda and Boyce, 1993). The Arruda–Boyce model has an additional material parameter, the limit stretch λ_m, which adjusts the range that strain-stiffening occurs and recovers the neo-Hookean model when the stretch is well below λ_m. When the stretch is comparable to the limit stretch, $\lambda \sim \lambda_m$, the stress in the Arruda–Boyce model increases sharply relative to the neo-Hookean model. At a given stretch, strain-stiffening increases with the decrease of λ_m. The formula of the Arruda–Boyce model as embedded in ABAQUS is used, but a user-defined material subroutine UMAT has been written to include the pre-stretch.

The pseudo-dynamic method is employed to study the formation and disappearance of ridges for different λ_m of the substrate, with $\mu_f/\mu_s = 1000$, $(h_f + h_s)/h_f = 200$ and $\lambda_0 = 2$. When $\lambda_m = 3$ in Fig. 13a, the wrinkle strain, the ridge to wrinkle transition, $\varepsilon_{r\to w}$, and the Maxwell strain, ε_{Max}, are not very different from the predictions for the neo-Hookean material, but the wrinkle to ridge transition strain, $\varepsilon_{w\to r}$, is 0.0253 which is considerably smaller than that for the neo-Hookean model (0.0361). With the decrease of λ_m to 2, $\varepsilon_{w\to r}$ decreases further and the separation between two transition strains becomes fairly small. For $\lambda_m = 1.5$, which is less than the pre-stretch $\lambda_0 = 2$, the separation vanishes and there is no longer hysteresis between the formation and disappearance of ridges. Ridges still form but the wrinkle to ridge transition becomes stable.

Fig. 13b shows the vertical displacement difference of the ridge peak during loading and unloading for $\lambda_m = 3$ and 1.5, with arrows showing the loading and unloading paths. When $\lambda_m = 3$, a clear hysteresis between loading and unloading is evident, while when $\lambda_m = 1.5$, the curves of loading and unloading superimpose. The height of the ridge, $V - V_0$, for $\lambda_m = 3$ is larger than $\lambda_m = 1.5$ under the same strain. The width of the ridges for $\lambda_m = 3$ is also larger than those for $\lambda_m = 1.5$, and therefore the aspect ratio of ridges do not change significantly. In the absence of hysteresis between the formation and disappearance of ridges for $\lambda_m = 1.5$, there is not a sharp indicator for the onset of ridges in Fig. 13b. A sharp indication of ridge formation is seen in Fig. 13c where the vertical displacement difference $V - V_0$ of the ridge peak and that of its neighboring wrinkle peak is plotted. This plot brings out the onset of localization associated with ridge formation.

In summary, the simulations in this section illustrate that details of ridge formation depend on the constitutive model invoked to characterize the substrate. While ridges as an advance mode are predicted by both constitutive models considered, the separation between the two transition strains, $\varepsilon_{r\to w}$ and $\varepsilon_{w\to r}$, and the associated hysteresis behavior depend on the details of the strain stiffening of the substrate.

4. Experiments

As discussed earlier, the wrinkle to ridge transition is unstable, and hysteresis exists in a closed loading/unloading cycle which spans $\varepsilon_{r\to w}$ and $\varepsilon_{w\to r}$. In this section, the transitions are studied experimentally with emphasis on the wrinkle to ridge transition and the hysteresis behavior.

A thin film/substrate system is realized by attaching a stiff polydimethylsiloxane (PDMS; Sylgard 184, Dow Corning) layer on a stretched soft PDMS substrate. The stiffness of the PDMS was varied by tuning its base/crosslinker ratio (5:1 for the stiff layer and 40:1 for the soft substrate). The film and substrate PDMS were spin-coated on glass substrates and cured for 2 h at 75 °C and for 1 h at 70 °C respectively. The shear modulus of the prepared film and substrate PDMS were 460KPa and 6KPa, respectively. The thickness of the stiff layer and the soft substrate were 7.3 μm and 500 μm, respectively. The substrate PDMS was cut into 20 mm width strips and removed from the glass substrate, then two opposing edges of the strip were clamped on a mechanical stage with the distance between the two edges 25 mm. The substrate was pre-stretched to $\lambda_o = 2$, and then the stress-free stiff layer was attached to the surface. For the attachment, we followed the method presented in (Chen and Crosby, 2014). The stiff layer was cut into squares of approximately 10 mm size, removed from the glass substrate, and floated on the water surface. Due to surface tension, folding of the stiff layer can be avoided with the layer remaining flat. The surface of the soft PDMS substrate is adhesive, and the substrate and the stiff layer were bonded simply by bringing them into contact. An overall compressive strain $\varepsilon = 15\%$ was gradually applied to the film/substrate system by partially releasing the pre-stretch of the substrate. Then, unloading back to $\varepsilon = 0$ was realized by re-stretching the substrate to the original pre-stretched state.

The surface morphology of the thin film/substrate was measured with an optical surface measurement system containing a microscope and a laser profiler (Keyence, VK-8710). Fig. 14 shows the top view of the surface under different compressive strains. The profiles of the surfaces measured by the laser profiler are also shown, and the vertical displacement difference between a peak of a wrinkle or ridge and the far field flat state, $V - V_0$, can be obtained from the measurement. Portions of the profile of the ridge were not captured because the laser cannot reflect from the inclined transparent surface of the ridge. The portions of the profiles of the ridge which cannot be properly measured were interpolated with dashed line in Fig. 14. Nevertheless, the position of the peak of the ridge and wrinkles, and therefore the vertical displacement difference $V - V_0$, were properly captured.

Under loading, wrinkles were clearly observed on the surface for compressive strains as large as $\varepsilon = 12.5\%$ (Fig. 14a). With further increase of the compressive strain to $\varepsilon = 15\%$, the deformation of the surface has localized at one of the wrinkle peaks forming a ridge (Fig. 14b). Then, unloading the compressive strain, the height of the ridge decreases (Fig. 14c).

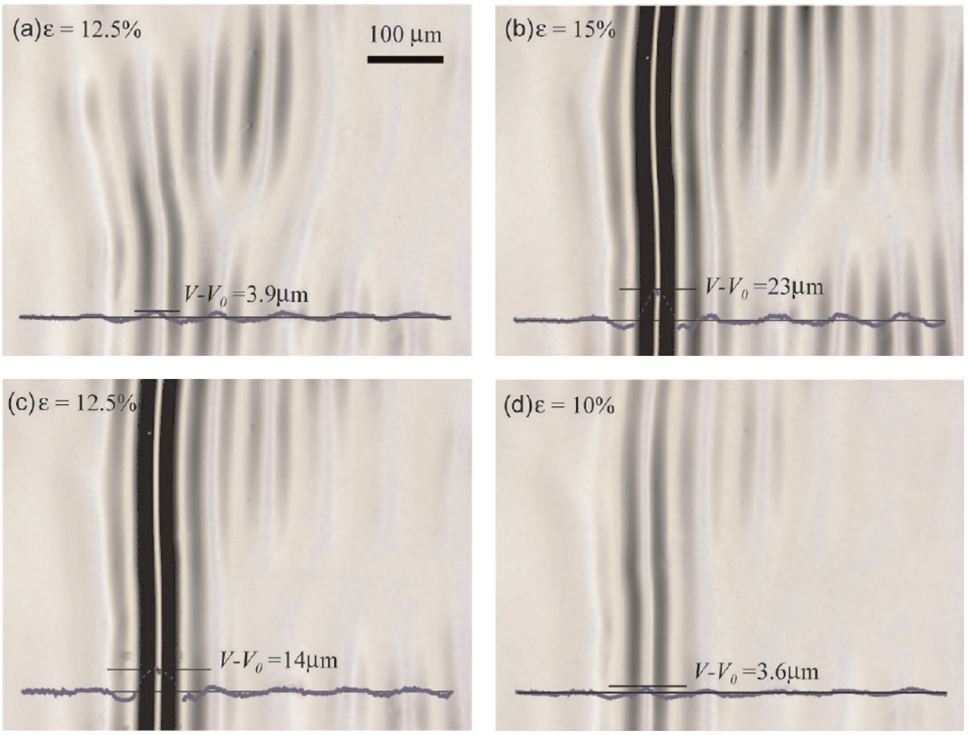

Fig. 14. Surface morphology of wrinkles and ridges under different overall compressive strains ε corresponding to loading in (a) and (b) and unloading in (c) and (d). The measured profiles of the surface indicated as dark lines are also shown in the images. (a) Wrinkles are clearly observed on loading to the compressive strain $\varepsilon = 12.5\%$. (b) With further loading to $\varepsilon = 15\%$ a localized ridge has formed. (c) Upon unloading back to $\varepsilon = 12.5\%$, a well-defined ridge exists but with decreased amplitude. Note that the two morphologies, wrinkles and ridges, exist at the same compressive strain $\varepsilon = 12.5\%$, one produced in loading and the other upon unloading, providing clear evidence of nonlinear hysteretic behavior. (d) Upon further unloading to $\varepsilon = 10\%$, the ridge has nearly transformed back to the wrinkled state.

Interestingly, the surface profiles at the same strain $\varepsilon = 12.5\%$ showing wrinkles in loading (Fig. 14a) and a ridge in unloading (Fig. 14c) provide a clear indication of the hysteresis between loading and unloading. With the further decrease of ε, the height of the ridge continues to decrease (Fig. 14d), and at $\varepsilon = 5\%$ the surface becomes almost flat again (not shown).

The vertical displacement difference $V - V_0$ as a function of strain ε is plotted in Fig. 15, with loading measurements represented by circles and unloading measurements represented by crosses. A strong hysteresis between the loading and

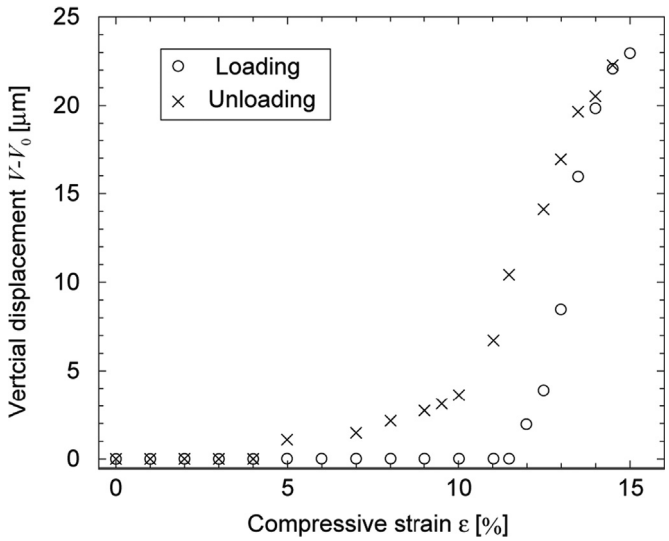

Fig. 15. The measured vertical displacement difference $V - V_0$ of the peak vertical displacement as a function of the compressive strain ε in loading and unloading showing clear evidence of the hysteretic behavior.

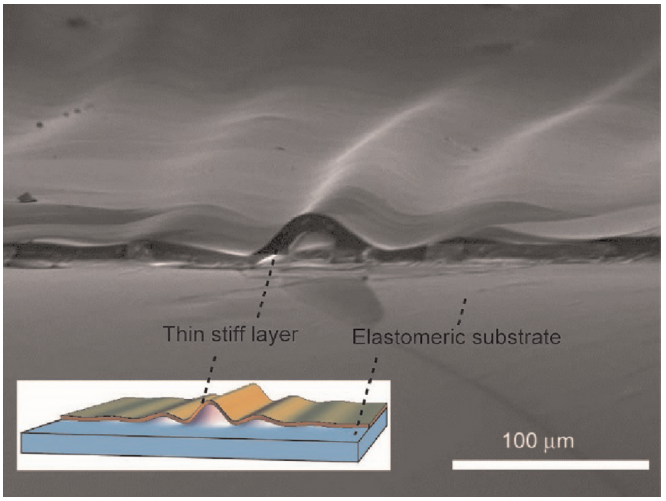

Fig. 16. SEM image of the ridge under strain $\varepsilon = 20\%$. This image is not a cross-sectional view of the bi-layer system, but a view of one of the unsupported sides of the bilayer where the ridge intersects the side.

unloading curves is observed, in qualitative agreement with the simulation results. For comparison purposes, plane strain simulations based on the neo-Hookean material model were carried out for parameter choices set to match the experimental system. The pre-stretch was set as $\lambda_o = 2$, the thickness ratio as $(h_f + h_s)/h_f = 50$, and the modulus ratio as $\mu_f/\mu_s = 30$ in order to match the experimental wrinkling strain $\varepsilon_w = 0.079$. The simulation predicts the transition strains: $\varepsilon_{r\to w} = 0.0864$ and $\varepsilon_{w\to r} = 0.0873$. Thus, while a hysteresis range emerges in both the simulations and the experiments, the strain range predicted by the simulation is much smaller than that observed experimentally in Fig. 15. Of the possible reasons for the quantitative discrepancy between the simulations and the experiments, we believe that two most important are: the experimental set-up produces states in the uniform state that are closer to uniaxial stress than to plane strain, and it is likely that stretch stiffening in the substrate PDMS is not correctly represented by the neo-Hookean model, as detailed in Section 3.4.

The profile of the ridge was also observed under a scanning electron microscope (SEM). Fig. 16 presents a ridge under strain $\varepsilon = 20\%$ viewed from the free edge of the film/substrate system. This perspective also reveals the localized nature of the ridge. Although not obvious in this view, it has been verified that the stiff layer remains attached to the elastomeric substrate. Debonding and interface sliding do not occur in the processes described above.

5. Conclusions

A study is presented of the mechanics of the formation of localized ridge instabilities which can occur in bilayer systems consisting of a thin stiff film on a compliant elastomeric substrate which has been pre-stretched prior to film attachment. The ridge is an advanced instability mode that occurs when the bilayer is compressed beyond the point at which sinusoidal wrinkles occur. Ridge formation is a localization process in the sense that one of the wrinkle peaks develops into the large amplitude ridge whose extra length of film is scavenged from neighboring wrinkles whose amplitudes become much smaller.

The simulations presented in this paper were all carried out in the context of two-dimensional plane strain. The nonlinearity of the phenomena requires specialized numerical methods and two particular methods have been employed here: the static force–displacement method and the pseudo-dynamic loading–unloading method. Two critical compressive strains have been identified and computed: the transition strain from wrinkles to ridges $\varepsilon_{w\to r}$ and the reverse transition strain from ridges to wrinkles $\varepsilon_{r\to w}$. There is a significant range of pre-stretch for which these two transition strains are distinct giving rise to strong hysteresis behavior in a cycle of loading and unloading. This range depends on the details of the substrate constitutive model and, in particular, on the stretch stiffening in the range of pre-strains. Loading from the flat state by increasing compression produces stable wrinkles followed by ridges at $\varepsilon_{w\to r}$. In the range of pre-stretch in which cyclic hysteresis exists, the wrinkle to ridge transition is unstable (sub-critical) with wrinkles snapping dynamical to ridges. Then, during unloading with decreasing compression, the ridges remain stable to compressive strains below $\varepsilon_{w\to r}$ until the ridge-to-wrinkle transition is reached at $\varepsilon_{r\to w}$ ($\varepsilon_{r\to w} < \varepsilon_{w\to r}$). Ridges do not exist at strains below $\varepsilon_{r\to w}$. This behavior is illustrated by the example in Fig. 6. The experiments reported in Section 4, in which the bilayer experiences conditions closer to uniaxial straining than plane strain, qualitatively reproduce the two distinct transition strains and associated hysteretic behavior under a cycle of loading and unloading.

The two-dimensional plane strain simulations have also been used to predict the Maxwell compressive strain ε_{Max} at which the energy in the wrinkle state is equal to that in the ridge state. In principle, the two states could co-exist at the Maxwell strain and, moreover, this would be the strain at which three-dimensional quasi-static propagation of ridges could occur. For the parameter range of the bilayers studied here, the Maxwell strain is only slightly larger than the lower of the two transition strains, $\varepsilon_{r\to w}$. Nevertheless, the experiments show that during the loading cycle the wrinkles are stable well beyond $\varepsilon_{r\to w}$. In other

words, even though ridges are energetically favorable at compressive strains above ε_{Max}, once wrinkles have formed and completely covered the surface of the bilayer they persist to considerably larger compressions approaching $\varepsilon_{w\to r}$. This is consistent with the plane strain simulations. The stability of the wrinkle mode in the experiments to compressive strains well above ε_{Max} implies that there must be a substantial energy barrier between the wrinkle and ridge states in the range $\varepsilon_{r\to w} < \varepsilon < \varepsilon_{w\to r}$. Conversely, once the ridges have formed they persist under unloading to the lower transition strain $\varepsilon_{r\to w}$. The existence of an energy barrier between the two states is clearly revealed in Fig. 3c for the specific case of the probing displacement Δ applied to the ridge peak. Other than this and the indirect evidence from the experiments, this paper has not directly addressed the magnitude of the energy barrier that exists between the wrinkle and ridge states. An interesting further set of experiments and/or three-dimensional analysis would explore the level of perturbations or disturbances required to cause a wrinkled surface to turn into ridges at compressive strains in the range $\varepsilon_{Max} < \varepsilon < \varepsilon_{w\to r}$ when wrinkles are stable but ridges have lower energy. In conducting the experiments, an attempt was made to trigger a ridge in a field of wrinkles in this range of strain. The unsuccessful effort entailed an attempt to grasp a wrinkle peak with tweezers and pull it upwards away from the substrate so as to promote a ridge, but it was not possible to grab a wrinkle. If future experiments on this system are conducted, thought should be given to the possibility of designing a probe into the experimental apparatus which could trigger ridges.

References

Arruda, E.M., Boyce, M.C., 1993. A three-dimensional constitutive model for the large stretch behavior of rubber elastic materials. J. Mech. Phys. Solids 41, 389–412.

Audoly, B., Boudaoud, A., 2008. Buckling of a stiff film bound to a compliant substrate-Part I: formulation, linear stability of cylindrical patterns, secondary bifurcations. J. Mech. Phys. Solids 56, 2401–2421.

Auguste, A., Jin, L., Suo, Z., Hayward, R.C., 2014. The role of substrate pre-stretch in post-wrinkling bifurcations. Soft Matter 10, 6520–6529.

Balluffi, R.W., Allen, S.M., Carter, W.C., 2005. Kinetics of materials. Wiley-Interscience, Hoboken, New Jersey.

Bowden, N., Brittain, S., Evans, A.G., Hutchinson, J.W., Whitesides, G.M., 1998. Spontaneous formation of ordered structures in thin films of metals supported on an elastomeric polymer. Nature 393, 146–149.

Brau, F., Damman, P., Diamant, H., Witten, T.A., 2013. Wrinkle to fold transition: influence of the substrate response. Soft Matter 9, 8177–8186.

Brau, F., Vandeparre, H., Sabbah, A., Poulard, C., Boudaoud, A., Damman, P., 2011. Multiple-length-scale elastic instability mimics parametric resonance of nonlinear oscillators. Nat. Phys. 7, 56–60.

Breid, D., Crosby, A.J., 2011. Effect of stress state on wrinkle morphology. Soft Matter 7, 4490–4496.

Budiansky, B., 1974. Theory of buckling and post-buckling behavior of elastic structures. Adv. Appl. Mech. 14, 1–65.

Cai, S., Breid, D., Crosby, A.J., Suo, Z., Hutchinson, J.W., 2011. Periodic patterns and energy states of buckled films on compliant substrates. J Mech. Phys. Solids 59, 1094–1114.

Cao, C., Chan, H.F., Zang, J., Leong, K.W., Zhao, X., 2014. Harnessing localized ridges for high-aspect-ratio hierarchical patterns with dynamic tunability and multifunctionality. Adv. Mater 26, 1763–1770.

Cao, Y.P., Hutchinson, J.W., 2012. Wrinkling phenomena in neo-Hookean film/substrate bilayers. J. Appl. Mech. – Trans. ASME 79, 031019.

Chan, E.P., Smith, E.J., Hayward, R.C., Crosby, A.J., 2008. Surface wrinkles for smart adhesion. Adv. Mater 20, 711–716.

Chen, Y.C., Crosby, A.J., 2014. High aspect ratio wrinkles via substrate prestretch. Adv. Mater 26, 5626–5631.

Chung, J.Y., Youngblood, J.P., Stafford, C.M., 2007. Anisotropic wetting on tunable micro-wrinkled surfaces. Soft Matter 3, 1163–1169.

Holmes, D.P., Crosby, A.J., 2010. Draping films: a wrinkle to fold transition. Phys. Rev. Lett. 105, 038303.

Khang, D.Y., Jiang, H.Q., Huang, Y., Rogers, J.A., 2006. A stretchable form of single-crystal silicon for high-performance electronics on rubber substrates. Science 311, 208–212.

Kim, P., Abkarian, M., Stone, H.A., 2011. Hierarchical folding of elastic membranes under biaxial compressive stress. Nat. Mater. 10, 952–957.

Kim, P., Hu, Y.H., Alvarenga, J., Kolle, M., Suo, Z.G., Aizenberg, J., 2013. Rational design of mechano-responsive optical materials by fine tuning the evolution of strain-dependent wrinkling patterns. Adv. Opt. Mater. 1, 381–388.

Lee, S.G., Lee, D.Y., Lim, H.S., Lee, D.H., Lee, S., Cho, K., 2010. Switchable transparency and wetting of elastomeric smart windows. Adv. Mater 22, 5013–5017.

Lin, P.-C., Yang, S., 2007. Spontaneous formation of one-dimensional ripples in transit to highly ordered two-dimensional herringbone structures through sequential and unequal biaxial mechanical stretching. Appl. Phys. Lett. 90, 241903.

Lin, P.C., Vajpayee, S., Jagota, A., Hui, C.Y., Yang, S., 2008. Mechanically tunable dry adhesive from wrinkled elastomers. Soft Matter 4, 1830–1835.

Lin, P.C., Yang, S., 2009. Mechanically switchable wetting on wrinkled elastomers with dual-scale roughness. Soft Matter 5, 1011–1018.

Lu, C.H., Mohwald, H., Fery, A., 2007. A lithography-free method for directed colloidal crystal assembly based on wrinkling. Soft Matter 3, 1530–1536.

Nowinski, J.L., 1969. Surface instability of a half-space under high two-dimensional compression. J. Frankl. Inst. 288, 367–376.

Pocivavsek, L., Dellsy, R., Kern, A., Johnson, S., Lin, B.H., Lee, K.Y.C., Cerda, E., 2008. Stress and fold localization in thin elastic membranes. Science 320, 912–916.

Porter, D.A., Easterling, K.E., 1981. Phase Transformations in Metals and Alloys. van Nostrand Reinhold, Berkshire, England.

Schweikart, A., Fery, A., 2009. Controlled wrinkling as a novel method for the fabrication of patterned surfaces. Microchim. Acta 165, 249–263.

Stafford, C.M., Harrison, C., Beers, K.L., Karim, A., Amis, E.J., Vanlandingham, M.R., Kim, H.C., Volksen, W., Miller, R.D., Simonyi, E.E., 2004. A buckling-based metrology for measuring the elastic moduli of polymeric thin films. Nat. Mater. 3, 545–550.

Sun, J.Y., Xia, S.M., Moon, M.W., Oh, K.H., Kim, K.S., 2012. Folding wrinkles of a thin stiff layer on a soft substrate. Proc. R. Soc. A – Math. Phys. Eng. Sci. 468, 932–953.

Takei, A., Jin, L., Hutchinson, J.W., Fujita, H., 2014. Ridge localizations and networks in thin films compressed by the incremental release of a large equibiaxial pre-stretch in the substrate. Adv. Mater 26, 4061–4067.

van der Heijden, A.M.A., 2009. Elastic Stability of Solids and Structures. In: Koiter's, W.T. (Ed.), . Cambridge University Press, New York.

Wang, Q.M., Zhao, X.H., 2013. Phase diagrams of instabilities in compressed film-substrate systems. J. Appl. Mech. – Trans. ASME 81, 051004.

Yin, J., Yague, J.L., Eggenspieler, D., Gleason, K.K., Boyce, M.C., 2012. Deterministic order in surface micro-topologies through sequential wrinkling. Adv. Mater 24, 5441–5446.

Zang, J., Zhao, X., Cao, Y., Hutchinson, J.W., 2012. Localized ridge wrinkling of stiff films on compliant substrates. J. Mech. Phys. Solids 60, 1265–1279.

Zhang, Z., James, R.D., Muller, S., 2009. Energy barriers and hysteresis in martensitic phase transformations. Acta Mater. 57, 4332–4352.